Solvent-Induced Tuning of Internal Structure in a Protein Amyloid Protofibril

Anjali Jha,[†] Satya Narayan,[†] Jayant B. Udgaonkar,[‡*] and G. Krishnamoorthy[†*]
[†]Department of Chemical Sciences, Tata Institute of Fundamental Research, Mumbai, India; and [‡]National Centre for Biological Sciences, Tata Institute of Fundamental Research, Bangalore, India

ABSTRACT An important goal in studies of protein aggregation is to obtain an understanding of the structural diversity that is characteristic of amyloid fibril and protofibril structures at the molecular level. In this study, what to our knowledge are novel assays based on time-resolved fluorescence anisotropy decay and dynamic quenching measurements of a fluorophore placed at different specific locations in the primary structure of a small protein, barstar, have been used to determine the extent to which the protein sequence participates in the structural core of protofibrils. The fluorescence measurements reveal the structural basis of how modulating solvent polarity results in the tuning of the protofibril conformation from a pair of parallel β-sheets in heat-induced protofibrils to a single parallel β-sheet in trifluorethanol-induced protofibrils. In trifluorethanol-induced protofibrils, the single β-sheet is shown to be built up from in-register β-strands formed by nearly the entire protein sequence, while in heat-induced protofibrils, the pair of β-sheets motif is built up from β-strands formed by only the last two-third of the protein sequence.

INTRODUCTION

Amyloid aggregates are β-sheet aggregates formed by many different proteins. In some cases, they are associated with diseases; in other cases, they carry out useful physiological functions (1–4). Although amyloidogenic proteins can have completely different primary structures, they form amyloid aggregates that are structurally similar both externally, in the appearance of the fibers formed, and internally, in possessing a characteristic cross-β-sheet in which β-strands run orthogonal to and interstrand hydrogen bonding extends parallel to the fiber axis (5). With the availability of high-resolution structural information, it has, however, become clear that amyloid structures formed by different proteins are diverse in their conformations (6–9). Even the same protein or peptide can aggregate into multiple amyloid conformations (8–13), which in the case of the prion protein form the basis of heritable prion strains and transmission barriers (14–16). Understanding the structural origin of the conformational diversity of amyloid aggregates formed by a protein will lead to a better understanding of the physicochemical interactions that drive amyloid aggregation (11,17).

High-resolution structural characterization of the conformational diversity in amyloidlike aggregates has been restricted so far to the mature aggregates known as amyloid fibrils (18–20). It has been more difficult to carry out high-resolution structural characterization of the curvilinear amyloid protofibrils and spherical oligomers that are seen to form during the course of amyloid fibril formation (1,21–23), or for the wormlike fibrils seen to be formed by the prion protein, as well as by β-microglobulin (8). Although conformational heterogeneity in such aggregates has been identified (24–26), there is little understanding of how such heterogeneity is related to the primary structure of the protein. Understanding conformational diversity in amyloid protofibrils and oligomers is important not only because they are presumed to be the direct structural precursors of amyloid fibrils (22,23) but also because it appears that they, and not the fibrils, may be the toxic species in amyloid aggregate-associated diseases (1,27–29).

Many, if not most, proteins are capable of forming amyloidlike aggregates in vitro under specific conditions of pH, temperature, and ionic strength (30,31). This provides an opportunity to study the structural characteristics of aggregates by using a model protein such as barstar (25,32,33) (Fig. 1). Barstar, an 89-residue protein with no disulphide bond, is the intracellular inhibitor of the extracellular ribonuclease barnase in *Bacillus amyloliquefaciens*, Barstar forms molten-globule-like soluble oligomers (the A form) at low pH. NMR studies have shown that the core of the A form is formed by the last two-thirds of the primary structure (34). The A form can be transformed into protofibrils in various aggregation conditions (21,25,32,35). Fluorescence measurements have shown that the residue-specific pattern of side-chain dynamics in the A form is similar to that in protofibrils, a result consistent with the A form being the direct precursor of the protofibrils (33). Atomic force microscopy (AFM) (21,25,33) and transmission electron microscopy (21) studies have shown that barstar protofibrils are curvilinear fibrillar structures several hundred nanometers in length. Interestingly, protofibrils formed by barstar under different aggregation conditions differ in both external appearance and size, as well as in stability (21,25). Thus, amyloid protofibrils formed by barstar are a promising model system for studying the phenomenon of conformational heterogeneity in protofibrils of amyloid aggregates.

Submitted March 6, 2012, and accepted for publication July 11, 2012.

*Correspondence: jayant@ncbs.res.in or gk@tifr.res.in

Editor: Elizabeth Rhoades.

0006-3495/12/08/0797/10 $2.00
http://dx.doi.org/10.1016/j.bpj.2012.07.021

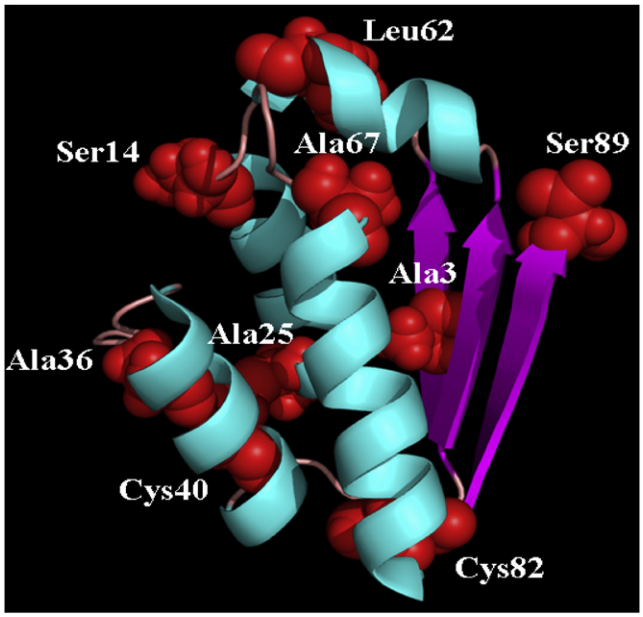

FIGURE 1 Crystal structure of barstar, and the locations of the nine different residues that were mutated to cysteine. The structure was drawn using PyMOL and the PDB file 1A19.

Of particular interest has been the observation that protofibrils formed by barstar in the presence of 10% (v/v) trifluoroethanol (TFE) at 25°C are structurally distinct from the heat-induced protofibrils formed in the absence of TFE at 70°C. In our earlier studies, it was shown that not only are the internal contents of β-structure different, as monitored by circular dichroism and Fourier-transform infrared spectroscopy, but more strikingly, the thickness of the TFE-induced protofibril is half that of the heat-induced protofibril, as monitored by AFM (21,25). It was also shown that only the lengths of the two types of protofibrils are similar, whereas the thickness of the TFE-induced protofibrils is similar to that of the single β-sheet in native barstar, and the thickness of the heat-induced protofibril is consistent with that of a pair of tightly mated β-sheets, as in a steric zipper (12). Understanding the differences in external morphology at the level of internal structure has, however, remained an unresolved problem.

In this study, it is first shown, using solution multiple-angle light scattering (MALS) as well as dynamic light scattering (DLS) measurements, that the TFE-induced protofibrils have half the molar mass of the heat-induced protofibrils, confirming the results of previous AFM measurements that the former have half the thickness of the latter. A novel, to our knowledge, time-resolved fluorescence anisotropy measurement assay was then used to delineate the sequence of the protein involved in forming the core of the TFE-induced protofibril structure. It is shown that nearly the entire protein sequence is involved in forming the core of the TFE-induced protofibril structure, whereas only the last two thirds of the sequence is involved in forming the core of the heat-induced protofibril structure. This result suggests that more extensive H-bonding might be the factor stabilizing the single β-sheet of TFE-induced protofibrils.

MATERIALS AND METHODS

Chemicals and buffers

All the chemicals used were of the highest purity grade available from Sigma Aldrich (St. Louis, MO). 5-((((2-iodoacetyl)amino)ethyl)amino) naphthalene-1-sulfonic acid (1,5-IAEDANS) was from Molecular Probes (Eugene, OR). The protein was dissolved initially in native buffer (pH 8.0). This was composed of 20 mM TRIS-HCl and 250 μM EDTA. All measurements were done at 23°C.

Protein expression and purification

The *Escherichia coli* strain used for protein expression was MM294. Wild-type barstar has two cysteine residues at positions 40 and 82. All the mutant versions of barstar used in this study contain a single cysteine at one of nine different locations and a single tryptophan (W53). The mutant proteins Cys-3, Cys-14, Cys-25, Cys-36, Cys-40, Cys-62, Cys-82, and Cys-89 were purified as described previously (32). Protein purity was checked by mass spectrometry using a Micromass Q-TOF Ultima mass spectrometer coupled with an ESI source. The purity of each protein was found to be >98%. Protein concentrations were determined by measuring the absorbance at 280 nm, using an extinction coefficient of 10,000 M^{-1} cm^{-1} for all the mutant proteins.

Preparation of labeled protein

For time-resolved fluorescence measurements, all the mutant proteins were labeled with the thiol labeling probe 1,5-IAEDANS in 7 M urea and 20 mM TRIS-HCl, pH 8, using a 20-fold molar excess of the dye in the dark. This reaction mixture was kept at room temperature for 5 h. After the labeling reaction was complete, the labeled protein was separated from free dye and urea by passing the reaction mixture through a PD-10 column (Pharmacia, Uppsala, Sweden). The extent of labeling was checked as in previous studies (32,33) and found to be >95% for all the mutant proteins.

Sample preparation and protofibrils formation from native protein

Purified labeled protein was concentrated using a Millipore (Billerica, MA) filter (5 kDa cut-off). A stock solution of 500 μM protein in 20 mM Tris-HCl buffer (pH 8.0) was made. MALS and DLS experiments indicate that the protein remains monomeric even at such a high concentration (data not shown). The concentration of protein was checked as described above. The stock solution of the 500-μM labeled native protein was diluted 10-fold into the 50 mM glycine buffer (pH 2.7) to give 50 μM of the A form (32). Similarly, a stock solution of the 20-μM labeled native protein was diluted 10-fold into the 50 mM glycine buffer (pH 2.7) to give 2 μM of the A form (32). The A form was incubated at room temperature for 30 min. The mixture of labeled and unlabeled protofibrils was prepared by mixing of the two stock solutions of 480 μM unlabeled and 20 μM labeled protein. This mixture was diluted 10-fold into the 50 mM glycine buffer (pH 2.7) to give the A form of the mixture (32).

The heat-induced protofibrils were formed by heat (70°C) treatment for 2.5 h of the A form at pH 2.7 in a dry bath (32). The protofibrils were brought back to room temperature after heating and incubated at room temperature for 10–15 min before data collection.

The TFE-induced protofibrils were formed from the A form by addition of TFE to a final concentration of 10% at 25°C (25). The final pH was 2.7. Aggregation was allowed to proceed at room temperature for 2 h.

Dynamic quenching experiments using acrylamide

Aqueous acrylamide solution was added to the labeled protofibril samples in the concentration range 0–600 mM. Fluorescence lifetimes were measured immediately after mixing. The bimolecular quenching constants (k_q) were estimated from the linear plot of τ_0/τ versus [Q], where τ_0 is the fluorescence lifetime in the absence of quencher and τ is the fluorescence lifetime in the presence of quencher at a concentration, [Q].

Time-resolved fluorescence measurements

Time-resolved fluorescence intensity and anisotropy decay kinetics experiments were carried out using a Ti-Sapphire picosecond laser and a time-correlated single-photon-counting (TCSPC) setup coupled to a microchannel plate photomultiplier as described earlier (33). Pulses of 1 ps duration of 820 nm radiation from the Ti-Sapphire laser were frequency-doubled to 410 nm using a frequency doubler (GWU, Spectra Physics, Santa Clara, CA). For all the time-resolved measurements, samples were excited at 410 nm at a pulse repetition rate of 4 MHz, and emission was measured at 525 nm. The instrument response function (IRF) was obtained at 410 nm using a very dilute colloidal suspension of dried nondairy coffee whitener. The width (full width at half-maximum) of the IRF was ~40 ps. The decay was deconvoluted with respect to the IRF and was analyzed using a sum of discrete exponentials, as described in the data analysis section. For the fluorescence lifetime measurements, peak counts of 10,000 were collected with the emission polarizer oriented at the magic angle (54.7°) with respect to the excitation polarizer. For time-resolved anisotropy measurements, the emission data were collected at 0° (parallel fluorescence intensity, $I_{||}$) and 90° (perpendicular fluorescence intensity, $I_{\perp}$) with respect to the excitation polarization (33).

Static and dynamic light scattering measurements

Simultaneous measurement of static light scattering at seven angles and DLS were performed using a DAWN 8+, eight-angle light-scattering instrument (Wyatt Technology, Santa Barbara, CA). Barstar samples (50 μM) in pH 2.7 buffer were either heated to 70°C (for heat-induced protofibrils) or mixed with TFE (10% v/v for TFE-induced protofibrils) and run through a 0.2-μm filter at a constant rate into the light-scattering flow cell. Normalization of the scattering intensity was done using a solution of bovine serum albumin.

Model used and data analysis

Fluorescence intensity decay curves were analyzed by deconvoluting the observed decay with the IRF to obtain the intensity decay function, represented as a sum of two or three exponentials as

$$I(t) = \Sigma\alpha_i \exp\left(\frac{-t}{\tau_i}\right) \quad \mathrm{i} = 2 \text{ or } 3, \tag{1}$$

where $I(t)$ is the fluorescence intensity collected at magic angle (54.7°) at time t, and α_i is the amplitude associated with the fluorescence lifetime, τ_i, such that $\sum \alpha_i = 1$. The mean lifetime, $\tau_m = \sum \alpha_i \tau_i$.

The time-resolved fluorescence anisotropy decays were analyzed by globally fitting $I_{ll}(t)$ and $I_{\perp}(t)$ as

$$I_{ll}(t) = \frac{I(t)[1 + 2r(t)]}{3} \tag{2}$$

$$I_{\perp}(t) = \frac{I(t)[1 - r(t)]}{3}, \tag{3}$$

where $I_{ll}(t)$ and $I_{\perp}(t)$ are the emission intensities collected at polarization directions parallel and perpendicular to the polarization of the excitation beam, and $r(t)$ is the anisotropy decay function, which is modeled in two different ways depending on the situation. For both types of protofibrils formed at high concentration of proteins (50 μM), it was analyzed as a sum of exponential terms:

$$r(t) = r_0 \sum \beta_j \exp\left(\frac{-t}{\phi_j}\right) \mathrm{j} = 2, \tag{4}$$

where r_0 is the limiting anisotropy in the absence of rotational diffusion, ϕ_j are the rotational correlation times with amplitudes β_j, such that $\sum \beta = 1$. This model assumes a population having uniform fluorescence dynamics properties, with each molecule associated with both the correlation times.

In contrast, the anisotropy decay kinetics of TFE and heat-induced protofibrils formed by 2-μM samples as well as mixed samples, which showed a dip-and-rise behavior, could not be fitted with the above model and requires a two-component model (32). This model assumes the presence of two populations, i.e., one of very small aggregates, and the other of larger aggregates (32). Furthermore, the rate of interconversion between the two populations is assumed to be slow when compared to the timescale of fluorescence lifetimes. In this model, each fluorophore population displays its own intensity and anisotropy decay kinetics (32). The time-dependent anisotropy is then given by

$$r(t) = f_1(t)r_1(t) + f_2(t)r_2(t), \tag{5}$$

where $f_1(t)$ and $f_2(t)$ are the fractions of the photons emitted by the very small and larger aggregates, respectively, at time t. $r_1(t)$ and $r_2(t)$ are the anisotropy decay functions of the two populations, respectively:

$$r_1(t) = r_0 \exp\left(\frac{-t}{\phi_{11}}\right) \tag{6}$$

$$r_2(t) = r_0\beta_{21} \exp\left(\frac{-t}{\phi_{21}}\right) + r_0\beta_{22} \exp\left(\frac{-t}{\phi_{22}}\right), \tag{7}$$

where $\beta_{21} + \beta_{22} = 1$

The anisotropy decay of the very small oligomers is described by a single rotational correlation time, ϕ_{11}. The higher oligomers are described by at least two rotational correlation times, ϕ_{21} and ϕ_{22}, with their amplitudes β_{21} and β_{22}, respectively.

The fractions $f_1(t)$ and $f_2(t)$ are given by

$$f_1(t) = \frac{\alpha_{11} \exp(-t/\tau_{11}) + \alpha_{12} \exp(-t/\tau_{12})}{\alpha_{11} \exp(-t/\tau_{11}) + \alpha_{12} \exp(-t/\tau_{12}) + \alpha_{21} \exp(-t/\tau_{21}) + \alpha_{22} \exp(-t/\tau_{22})} \tag{8}$$

$$f_2(t) = \frac{\alpha_{21} \exp(-t/\tau_{21}) + \alpha_{22} \exp(-t/\tau_{22})}{\alpha_{11} \exp(-t/\tau_{11}) + \alpha_{12} \exp(-t/\tau_{12}) + \alpha_{21} \exp(-t/\tau_{21}) + \alpha_{22} \exp(-t/\tau_{22})}, \tag{9}$$

where α_{11} and α_{12} are the relative amplitudes of the fluorescence lifetimes τ_{11} and τ_{12}, respectively, for population 1 (very small oligomers). Similarly, α_{21} and α_{22} are the amplitudes of the fluorescence lifetimes τ_{21} and τ_{22}, respectively, for population 2 (higher oligomers).

While analyzing the anisotropy decay traces using Eqs. 1–9, the parameters associated with the fluorescence intensity decay were kept fixed at the values obtained from the analysis of fluorescence intensity decays collected at the magic angle with respect to the excitation polarization. Furthermore, the initial anisotropy, r_0, was also estimated from an independent experiment in which the decay of the fluorescence anisotropy of the IAEDANS in 70% glycerol was measured and kept fixed at this value while analyzing the anisotropy decay kinetics of the protofibrils. These procedures enhanced the reliability of the estimates of the parameters associated with the anisotropy decay of protofibril samples. The goodness of fit was assessed from the values of the reduced chi-square (1.0–1.2) and randomness of residuals (32).

Dynamic quenching constant (k_q)

The bimolecular quenching constant (k_q) was estimated from the linear plot of τ_0/τ_m versus $[Q]$,

$$\frac{\tau_0}{\tau_m} = 1 + k_q \tau_0 [Q], \tag{10}$$

where τ_0 is the mean fluorescence lifetime in the absence of quencher and τ_m is the mean fluorescence lifetime in the presence of quencher at a concentration $[Q]$. The slope of the Stern-Volmer plot, i.e., the Stern-Volmer constant, K_{sv}, is equal to $k_q \times \tau_0$.

RESULTS AND DISCUSSION

Structural polymorphism in amyloid protofibrils

In previous AFM studies (21,25), it was shown that TFE-induced protofibrils had half the thickness of heat-induced protofibrils, and it was suggested that the former was formed from a single β-sheet, whereas the latter was formed from a pair of tightly mated β-sheets. Since the canonical structure for amyloid fibrillar structures is a pair of tightly mated β-sheets (2,4,12,19), and since it is very unusual for the TFE-induced protofibrils to have been formed from only a single β-sheet, it became necessary to show that the AFM-determined thickness of the TFE-induced protofibrils is not an artifact of measurements made on a dry mica surface to which the protofibrils had been bound for the AFM. Hence, light-scattering experiments, MALS as well as DLS measurements, have been used in this study to demonstrate that even though the TFE-induced and heat-induced protofibrils are of the same length in solution, the former have half the molar mass of the latter. Fig. 2 *A* shows that when the time evolution of molar mass during protofibril formation is monitored by measurement of the static light-scattering intensities at seven angles simultaneously, the weight-averaged molar mass of the heat-induced protofibrils is found to reach a value that is approximately twofold higher than that of the TFE-induced protofibrils. On the other hand, the hydrodynamic radius (R_h), estimated from simultaneous measurement of DLS, increases with similar kinetics to very similar saturation values for both types of protofibrils (Fig. 2 *B*). The twofold larger molar mass of the heat-induced protofibrils is in line with the twofold greater thickness of the heat-induced protofibrils observed earlier by AFM (25). The values of R_h for both types of protofibrils are similar, because the lengths of the protofibrils, which are similar, dominate over their thicknesses in giving rise to the effective value of R_h (36). The slightly larger value of R_h observed for the TFE-induced protofibril may be due to the fact that the length of its core region, which would correspond to the width of the protofibril, is larger than that of the heat-induced protofibril (as discussed below). In the absence of TFE, heat-induced protofibrils form 200 times more slowly at 25°C than at 70°C, but they have the same thickness of a pair of β-sheets as shown by earlier AFM work (37). Although these studies confirm the difference in gross morphologies of the protofibrils formed under the two different aggregation conditions, they give little insight into the differences in the internal structures of the two protofibrils.

Internal structure of TFE- and heat-induced protofibrils

To gain more insight into the structures of these two types of protofibril, the internal structure of the TFE-induced

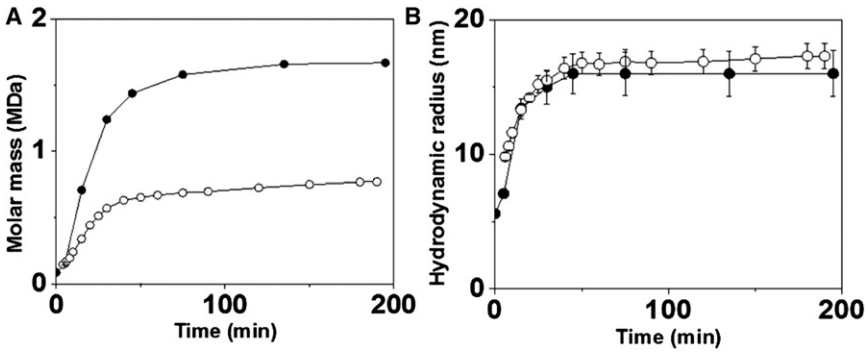

FIGURE 2 Time evolution of weight-averaged molar mass, estimated by seven-angle static light scattering measurement (*A*), and hydrodynamic radius, estimated by simultaneous DLS measurement (*B*) during the formation of protofibrils of barstar either in the absence of any added cosolvent at 70°C (heat-induced; *solid circles*) or in the presence of the cosolvent TFE (10%) at 25°C (TFE-induced; *open circles*). The error bars are smaller than the size of the symbols in *A*. The heat-induced protofibrils were formed by heat treatment (70°C) for 2.5 h of the A form at pH 2.7 in a dry bath (33). The protofibrils were brought back to room temperature after heating, and incubated at room temperature for 10–15 min before data collection. The TFE-induced protofibrils were formed from the A form by addition of TFE to a final concentration of 10% at 25°C (26). The final pH was 2.7. Aggregation was allowed to proceed at room temperature for 2 h.

protofibrils was probed in a site-specific manner using fluorescence anisotropy decay kinetics, and it is compared with that of the heat-induced protofibrils characterized in an earlier study (32). Amyloid protofibril formation by nine single cysteine-containing mutant forms of barstar (Fig. 1) was studied. The selected residue positions (3, 14, 25, 36, 40, 62, 67, 82, and 89) scan the entire primary structure of the protein. Each protein was labeled at its sole cysteine thiol with 1,5-IAEDANS. Fig. 3 shows the fluorescence anisotropy decay kinetics of the TFE-induced protofibrils for nine 1,5-IAEDANS-labeled single-cysteine mutant forms of barstar. The fluorescence anisotropy decay of protofibrils formed from 50 μM labeled barstar (Fig. 3, *green traces*) shows two phases representing the local motion of the probe and global dynamics of the entire protofibril, as expected (32). Parameters obtained from fitting are listed in Table 1. The difference in the decay parameters of the various mutant proteins is due to differences in rigidity along the sequence, as observed in our earlier work (33). Cys-3 shows more flexibility when compared to the other proteins (Table 1). In contrast to this series of samples, protofibrils formed from 2 μM of some of the mutant proteins (e.g., Fig. 3, *black traces* for Cys-82) shows a dip-and-rise behavior in fluorescence anisotropy decay. This behavior arises because at the low protein concentration, the protofibril population exists along with a population of smaller aggregates with significantly different fluorescence properties (32). Parameters obtained from fitting are listed in Table 2). The model used for the analysis of such behavior and its mathematical treatment are described in the Materials and

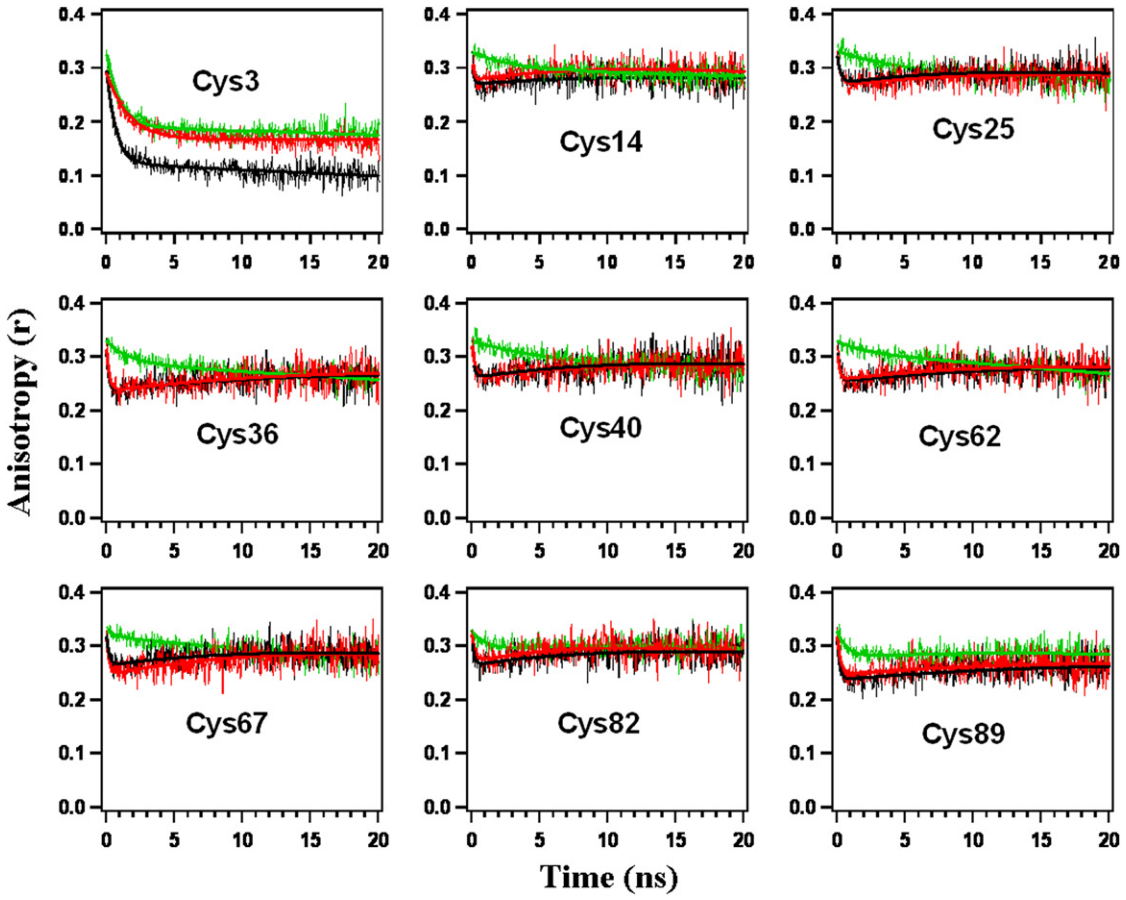

FIGURE 3 Fluorescence **a**nisotropy decay kinetics of the fluorophore in the protofibrils formed from the nine different mutant proteins at different concentrations. Each panel shows kinetic decays for TFE-induced protofibrils. The protein was incubated with 10% TFE at pH 2.7, 25°C. Each panel shows the anisotropy decay kinetics for the protofibrils formed by 50 μM of the labeled protein (*green line*), 2 μM of the labeled protein (*black line*), and a mixture of 2 μM of the labeled protein and 48 μM of the unlabeled protein (*red line*). The smooth lines are the fits to Eqs. 1–9. The parameters obtained from the fitting of decay kinetics of TFE-induced protofibrils are listed in Tables 2–4. Time-resolved fluorescence intensity and anisotropy decay kinetics experiments were carried out using a Ti-Sapphire picosecond laser and a time-correlated single-photon-counting setup, coupled to a microchannel plate photomultiplier. For details, see Materials and Methods. The protofibrils were formed at a high (50 μM) concentration of proteins. Each anisotropy decay was analyzed as a sum of exponential terms, $r(t) = r_0 \sum \beta_j \exp(-t/\phi_j)$, $j = 2$, where r_0 is the limiting anisotropy in the absence of rotational diffusion and ϕ_j are the rotational correlation times with amplitudes β_j, such that $\sum \beta_j = 1$. This model assumes a population having uniform fluorescence dynamics properties, with each molecule associated with both the correlation times. In contrast, the anisotropy decay kinetics of TFE-induced protofibrils formed by 2-μM samples, as well as mixed samples, which showed a dip-and-rise behavior, are fitted with a two-component model (33). For details, see Materials and Methods.

TABLE 1 Rotational correlation times (ϕ) and their amplitudes (β) in TFE-induced protofibrils of nine mutant proteins labeled with 1,5-IAEDANS

	TFE-induced protofibrils	
Mutant	ϕ_1 (ns) (β_1)	ϕ_2 (ns) (β_2)
Cys-3	1.6 (0.19), 0.2 (0.26)	>200 (0.55)
Cys-14	2.3 (0.11)	>200 (0.89)
Cys-25	3.0 (0.09)	>200 (0.91)
Cys-36	2.8 (0.08)	>200 (0.92)
Cys-40	3.2 (0.09)	>200 (0.91)
Cys-62	2.8 (0.11)	>200 (0.89)
Cys-67	2.9 (0.10)	>200 (0.90)
Cys-82	3.1 (0.10)	>200 (0.90)
Cys-89	2.3 (0.15)	>200 (0.85)

Concentration of the proteins was 50 μM. Fluorescence anisotropy decay kinetics were analyzed using Eqs. 1–4. Errors associated with each measurement are <10%.

Methods section. More details of the methodology are also explained elsewhere (32).

The identification of polypeptide sites involved in protofibril core formation comes from the fluorescence anisotropy decay curves of mixtures of 2 μM labeled protein and 48 μM of unlabeled protein (32). Parameters obtained from fitting are listed in Table 3. If the labeled and unlabeled proteins interact with each other and form coprotofibrils, then the fluorescence anisotropy decay kinetics of the mixture would be similar to that observed with 50 μM of labeled protein, as they are for Cys-3 (Fig. 3). Alternatively, if the labeled and unlabeled proteins do not interact with each other (due to the label being present at the interacting core region), and instead form two separate populations of protofibrils, the observed anisotropy decay kinetics of the mixture would be similar to that of the 2 μM labeled protein, as seen for Cys-82 (Fig. 3). The inability of the fluorescently labeled and unlabeled proteins to interact with each other when the fluorophore is attached to the core region is indicative of crystal-like packing in the protofibril core region, as suggested in an earlier study (12). In the case of heat-induced protofibrils, the approach detailed above showed that about two-thirds of the protein sequence at the C-terminal end is involved in the formation of the protofibril core while the remaining one-third (the N-terminal region) remains noninteractive and largely flexible (32).

In this work, a similar evaluation was carried out for the TFE-induced protofibrils. Inspection of the traces shown in Fig. 3 shows that for the TFE-induced protofibrils, the dip-and-rise fluorescence anisotropy decay behavior of the mixture (2 μM of labeled protein and 48 μM of unlabeled protein) is similar to that of the 2-μM labeled sample when the label is present at any of the residue positions 14, 25, 36, 40, 62, 67, 82, and 89. The dip-and-rise behavior is not seen when the label is present at residue position 3. These results are interpreted as indicating that the region 14–89, but not the preceding region, is involved in the formation of ordered structure. In contrast, the ordered region for the heat-induced protofibrils is 36–89 (32) (Figs. 3 and 4).

The inferred enlargement of the ordered region in the TFE-induced protofibril compared to that in the heat-induced protofibril indicates internal structural differences between the two forms of protofibril. To get more insight, the solvent accessibilities of various residues along the length of the polypeptide were determined by measurement of the dynamic fluorescence quenching (38) of the fluorescent label placed at each of the nine residue positions. An earlier study had shown that acrylamide can be used as an efficient quencher of the fluorescence of 1,5-IAEDANS (33). Details of the experimental methodology used here are presented in the Materials and Methods section . Bimolecular quenching constants, k_q, estimated from these plots are given in Table 4. It is worth mentioning that k_q estimated from the mean lifetime (when the decay is multiexponential) cannot strictly be called the bimolecular quenching constant. The apparent value of k_q estimated in this way can, however, be used in a comparative sense, as we have done in this work. These estimates show that for

TABLE 2 Parameter obtained from fitting at low protein concentration

		Population 1			Population 2			
		Fluorescence lifetimes (ns)		Rotational correlation time (ns)	Fluorescence lifetimes (ns)		Rotational correlation times (ns)	
Proteins	Fraction of population 1	τ_{11} (α_{11})	τ_{12} (α_{12})	ϕ_{11}	τ_{21} (α_{21})	τ_{22} (α_{22})	ϕ_{21} (β_{21})	ϕ_{22} (β_{22})
Cys-3	0.25	8.6 (0.83)	0.45 (0.17)	0.77	9.7 (0.20)	23 (0.80)	2.1 (0.07)	~65 (0.93)
Cys-14	0.25	7.7 (0.85)	0.65 (0.15)	0.81	9.2 (0.08)	25 (0.92)	2.2 (0.08)	>100 (0.92)
Cys-25	0.27	7.5 (0.80)	0.39 (0.20)	0.83	9.4 (0.11)	27 (0.89)	2.1 (0.08)	>100 (0.92)
Cys-36	0.29	8.2 (0.82)	0.48 (0.18)	0.84	9.1 (0.13)	29 (0.87)	2.5 (0.05)	>100 (0.95)
Cys-40	0.25	7.4 (0.78)	0.67 (0.22)	0.64	8.7 (0.15)	29 (0.85)	2.4 (0.08)	>100 (0.92)
Cys-62	0.28	7.1 (0.76)	0.63 (0.24)	0.67	8.7 (0.25)	29 (0.75)	1.7 (0.05)	>100 (0.95)
Cys-67	0.27	6.9 (0.73)	0.69 (0.27)	0.56	8.6 (0.24)	28 (0.76)	1.5 (0.06)	>100 (0.94)
Cys-82	0.26	7.4 (0.70)	0.54 (0.30)	0.59	8.1 (0.22)	25 (0.78)	1.4 (0.05)	>100 (0.95)
Cys-89	0.27	6.6 (0.65)	0.48 (0.35)	0.49	7.4 (0.30)	23 (0.70)	1.5 (0.08)	>100 (0.92)

Values given in parentheses are amplitudes for the fluorescence lifetimes (τ). The concentration of the proteins was 2 μM. Fluorescence anisotropy decay kinetics were analyzed using Eqs. 5–9. Errors associated with each measurement are <10%.

TABLE 3 Fluorescence anisotropy decay measured with the TFE-induced protofibrils formed by the mixed proteins

		Population 1			Population 2			
		Fluorescence lifetimes (ns)		Rotational correlation time	Fluorescence lifetimes (ns)		Rotational correlation times (ns)	
Proteins	Fraction of population 1	τ_{11} (α_{11})	τ_{12} (α_{12})	ϕ_{11}	τ_{21} (α_{21})	τ_{22} (α_{22})	ϕ_{21} (β_{21})	ϕ_{22} (β_{22})
Cys-3	0.08	3.9 (1.0)	—	1.20	11.1 (0.30)	19.2 (0.70)	1.9 (0.10)	>100 (0.90)
Cys-14	0.26	7.5 (0.87)	0.61 (0.13)	0.75	9.1 (0.10)	27 (0.90)	2.1 (0.10)	>100 (0.90)
Cys-25	0.26	7.5 (0.82)	0.45 (0.18)	0.79	9.2 (0.12)	28 (0.88)	2.0 (0.09)	>100 (0.91)
Cys-36	0.30	7.9 (0.80)	0.51 (0.20)	0.82	9.2 (0.13)	27 (0.87)	2.2 (0.05)	>100 (0.95)
Cys-40	0.27	7.5 (0.79)	0.70 (0.21)	0.67	8.9 (0.14)	29 (0.86)	2.4 (0.08)	>100 (0.92)
Cys-62	0.27	6.8 (0.76)	0.59 (0.24)	0.65	8.5 (0.23)	29 (0.77)	1.9 (0.06)	>100 (0.94)
Cys-67	0.26	6.2 (0.74)	0.67 (0.26)	0.55	8.6 (0.23)	29 (0.77)	1.6 (0.08)	>100 (0.92)
Cys-82	0.26	7.1 (0.63)	0.55 (0.33)	0.58	8.2 (0.22)	27 (0.78)	1.5 (0.05)	>100 (0.95)
Cys-89	0.26	6.1 (0.63)	0.46 (0.37)	0.50	7.2 (0.29)	25 (0.71)	1.4 (0.10)	>100 (0.90)

Values given in parentheses are amplitudes for the fluorescence lifetimes (τ). Proteins were a mixture of 2 μM IAEDANS-labeled protein + 48 μM of unlabeled protein, and were analyzed using Eqs. 5–9. Errors associated with each measurement are <10%.

the TFE-induced protofibrils, only the Cys-3 variant shows a high value for quenching rate constant ($k_q \sim 2.65 \times 10^8$ M^{-1} s^{-1}), whereas the other eight mutant forms show relatively smaller values of k_q ($<0.86 \times 10^8$ M^{-1} s^{-1}). The low level of solvent accessibility for the region 14–89 indicates that this is the well-packed core segment. In contrast, in the case of the heat-induced protofibrils, the values of k_q for the region 3–25 are higher than those for the region 36–89, indicating that the latter region is the core segment. This result is similar to our earlier observations (32). Thus, both the fluorescence anisotropy decay measurements and the dynamic quenching measurements suggest that a larger segment of the polypeptide chain (14–89) participates in the amyloid protofibril core in the case of the TFE-induced protofibrils than in the case of the heat-induced protofibrils, where only the sequence segment 36–89 participates. It could be argued that the IAEDANS probe should be accessible to the solvent even when it is

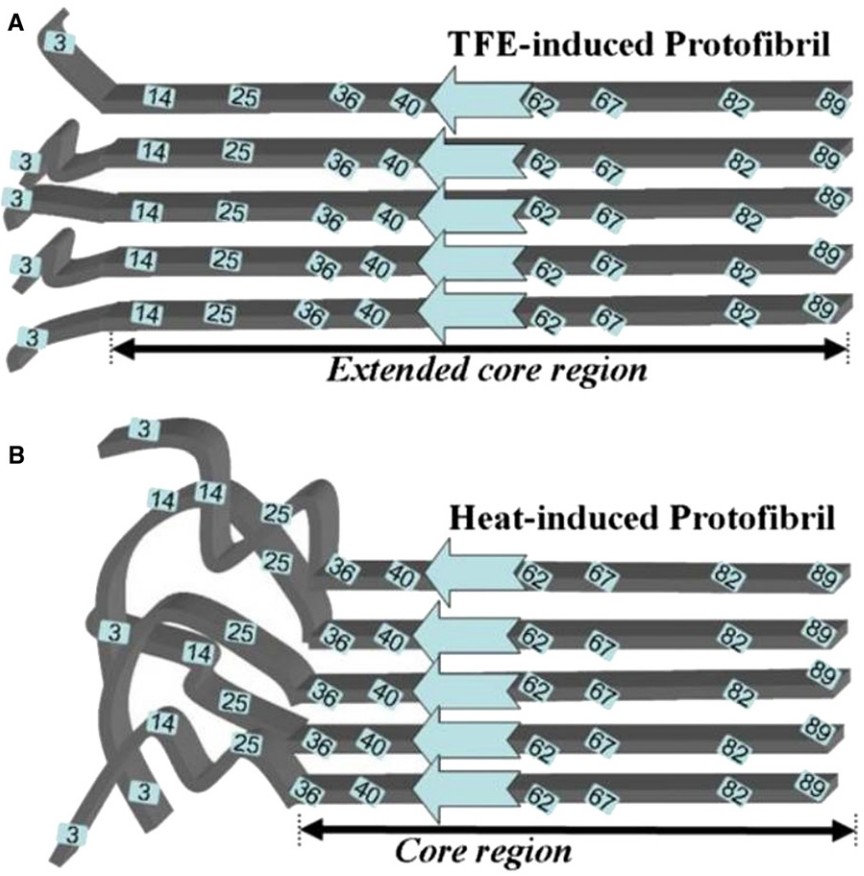

FIGURE 4 Models for the β-sheet structures of TFE-induced (*A*) and heat-induced protofibrils (*B*). Self-complementary interactions in the rigid core region point toward an in-register parallel organization of the polypeptide β-strands. The model for TFE-induced protofibrils in *A* shows that residues 14–89 participate in specific interpeptide interstrand interactions. The model for heat-induced protofibrils in *B* shows that only residues 36–89 participate in specific interpeptide interactions.

TABLE 4 Acrylamide quenching of the fluorescence of IAEDANS attached to a single cysteine thiol in TFE- and heat-induced protofibrils

	$k_q \times 10^8$ (M^{-1} s^{-1})	
Mutant variants	TFE-induced protofibril	Heat-induced protofibril
Cys-3	2.65	3.09
Cys-14	0.86	2.21
Cys-25	0.65	1.93
Cys-36	0.52	1.11
Cys-40	0.54	0.57
Cys-62	0.71	0.78
Cys-67	0.52	0.72
Cys-82	0.64	0.55
Cys-89	0.68	0.73

Values are for protofibrils formed by all nine mutant variants of barstar. The bimolecular quenching rate constant (k_q) was obtained by analyzing the Stern-Volmer plots using Eq. 10.

packed in the β-sheet. The observed three- to fourfold reduction in the value of k_q, but not a complete abolition of quenching, indicates that the probe is only partially hindered with respect to solvent accessibility, remaining tightly packed in the core of the fibril.

Structure and stability of monolayer TFE-induced protofibrils and bilayer heat-induced protofibrils

Previous studies have indicated that β-sheet is formed when protofibril formation is induced, either by heat or by TFE (21,25,37). In the case of heat-induced protofibrils, the inability of the protein labeled at any of the residue positions 36–89 to cofibrillate with its unlabeled counterpart led to a model in which sequence segments 36–89 from different protein molecules assemble orthogonal to the protofibril axis, to form an in-register parallel β-sheet (32). The thickness of the protofibril indicated that a pair of β-sheets formed in this manner extends parallel to the protofibril axis. In the case of TFE-induced protofibrils, a similar interpretation of the data presented here indicates that sequence segments 14–89 from different protein molecules assemble orthogonal to the protofibril axis to form an in-register parallel β-sheet. The light-scattering data presented here (Fig. 2), as well as the earlier AFM data, indicate, however, that the parallel β-sheet extending in the direction of the protofibril axis remains a single layer.

It appears that for both types of protofibrils, interstrand interactions between adjacent identical residues play a dominant role in determining the specificity with which β-strands assemble to form the in-register parallel β-sheet. This specificity is remarkable: when a residue in the core region is labeled with the fluorophore, the resultant labeled molecules cannot cofibrillate with their unlabeled counterparts. Since adjacent residues in a parallel β-sheet do not hydrogen-bond with each other at the main chain level, it appears that self-complementary side-chain interactions between opposing residues play a major role in determining the extent to which the primary structure participates in the β-sheet core of the amyloid fibril. Intrasheet side-chain packing interactions, as well as electrostatic interactions, between adjacent residues in a parallel β-sheet are known to contribute to the stability of the β-sheet (39), and the importance of such interstrand interactions is reflected in the amino acid pairing preferences that have been discerned in parallel β-sheets (40). The high level of pairwise preference for the residue in the adjacent chain (40) could be the driving force for the absence of cofibril formation when the fluorophore is introduced in the interacting core region of one of the interacting peptides.

The canonical motif of amyloid fibril structure, deduced from the structures of many different amyloidogenic peptides in crystalline form, is a pair of β-sheets that may (12) or may not (11) form intersheet steric zippers. The pair-of-β-sheets motif appears to be stabilized by intersheet hydrophobic, aromatic, electrostatic, and packing interactions (3,11,12,19,41–44). The heat-induced protofibrils of barstar would be stabilized by such intersheet interactions. In the case of the TFE-induced protofibrils, the origin of the stability of the monolayer β-sheet structure would lie in the extended core region (residues 14–89) compared to that present in heat-induced protofibrils (residues 36–89) (Fig. 4). The extent of interstrand hydrogen bonding would be greater, because the lengths of the β-strands in the parallel β-sheet forming the core region are longer. It should be noted that earlier circular dichroism and Fourier-transform infrared spectroscopy studies indicated that the β-sheet content is greater in TFE-induced protofibrils than in heat-induced protofibrils (25). In this study, the extent to which the β-sheet content is greater has been delineated at the amino acid residue level.

The effect of TFE is remarkable but perhaps not surprising in retrospect. TFE decreases solvent polarity (45,46); consequently, hydrogen-bonding interactions are enhanced. Hence, the presence of TFE as a cosolvent increases helical content in some cases (47), and β-sheet, as well as β-turn, content in other cases (48,49). It is therefore likely that the enhancement of hydrogen-bonding interactions by TFE confers sufficient additional stability for a longer monolayer β-sheet to be stable by itself. The lower solvent polarity in the presence of TFE also results in a decrease in hydrophobic interactions (45,46,50). A TFE-caused weakening of hydrophobic interactions between two layers of β-sheet might be responsible for the absence of the pair-of-β-sheets motif in the TFE-induced protofibrils. The dual effects of TFE are responsible for its dramatic ability to tune the structure of protofibrils from a pair of β-sheets in its absence to a single β-sheet in its presence.

In summary, by examining, at individual residue resolution, the structures of two types of fibril grown in different aggregation conditions, this study shows that protofibril formation and structure are controlled by a fine balance of

different stabilizing and destabilizing physical forces. In different aggregation conditions, different physical forces dominate, thereby affecting both side-chain and main-chain structure. This study suggests that intrasheet interstrand side-chain interactions play a fundamental role in protofibril structure and are responsible for structural differences in protofibrils at the individual residue level. Modulating interstrand side-chain, as well as main-chain, interactions by tuning the properties of the solvent leads to amyloid protofibrils of fundamentally different internal structure and, hence, different external morphology.

We thank Prof. N. Periasamy for the software used in the analysis of time-resolved fluorescence data.

This work was funded by the Tata Institute of Fundamental Research, and by the Department of Biotechnology, government of India. G.K. and J.B.U. are recipients of J. C. Bose National Research Fellowships from the government of India.

REFERENCES

1. Caughey, B., and P. T. Lansbury. 2003. Protofibrils, pores, fibrils, and neurodegeneration: separating the responsible protein aggregates from the innocent bystanders. *Annu. Rev. Neurosci.* 26:267–298.
2. Chiti, F., and C. M. Dobson. 2006. Protein misfolding, functional amyloid, and human disease. *Annu. Rev. Biochem.* 75:333–366.
3. Wickner, R. B., F. Shewmaker, …, C. L. Winchester. 2010. Prion amyloid structure explains templating: how proteins can be genes. *FEMS Yeast Res.* 10:980–991.
4. Greenwald, J., and R. Riek. 2010. Biology of amyloid: structure, function, and regulation. *Structure.* 18:1244–1260.
5. Sunde, M., L. C. Serpell, …, C. C. Blake. 1997. Common core structure of amyloid fibrils by synchrotron x-ray diffraction. *J. Mol. Biol.* 273: 729–739.
6. Bauer, H. H., U. Aebi, …, H. P. Merkle. 1995. Architecture and polymorphism of fibrillar supramolecular assemblies produced by in vitro aggregation of human calcitonin. *J. Struct. Biol.* 115:1–15.
7. Goldsbury, C., P. Frey, …, S. A. Müller. 2005. Multiple assembly pathways underlie amyloid-beta fibril polymorphisms. *J. Mol. Biol.* 352: 282–298.
8. Gosal, W. S., I. J. Morten, …, S. E. Radford. 2005. Competing pathways determine fibril morphology in the self-assembly of β2-microglobulin into amyloid. *J. Mol. Biol.* 351:850–864.
9. Petkova, A. T., R. D. Leapman, …, R. Tycko. 2005. Self-propagating, molecular-level polymorphism in Alzheimer's β-amyloid fibrils. *Science.* 307:262–265.
10. Madine, J., E. Jack, …, D. A. Middleton. 2008. Structural insights into the polymorphism of amyloid-like fibrils formed by region 20–29 of amylin revealed by solid-state NMR and x-ray fiber diffraction. *J. Am. Chem. Soc.* 130:14990–15001.
11. Marshall, K. E., K. L. Morris, …, L. C. Serpell. 2011. Hydrophobic, aromatic, and electrostatic interactions play a central role in amyloid fibril formation and stability. *Biochemistry.* 50:2061–2071.
12. Sawaya, M. R., S. Sambashivan, …, D. Eisenberg. 2007. Atomic structures of amyloid cross-β spines reveal varied steric zippers. *Nature.* 447:453–457.
13. Dupuis, N. F., C. Wu, …, M. T. Bowers. 2011. The amyloid formation mechanism in human IAPP: dimers have β-strand monomer-monomer interfaces. *J. Am. Chem. Soc.* 133:7240–7243.
14. Apostol, M. I., J. J. Wiltzius, …, D. Eisenberg. 2011. Atomic structures suggest determinants of transmission barriers in mammalian prion disease. *Biochemistry.* 50:2456–2463.
15. Toyama, B. H., and J. S. Weissman. 2011. Amyloid structure: conformational diversity and consequences. *Annu. Rev. Biochem.* 80: 557–585.
16. Wiltzius, J. J., M. Landau, …, D. Eisenberg. 2009. Molecular mechanisms for protein-encoded inheritance. *Nat. Struct. Mol. Biol.* 16: 973–978.
17. Schmit, J. D., K. Ghosh, and K. Dill. 2011. What drives amyloid molecules to assemble into oligomers and fibrils? *Biophys. J.* 100:450–458.
18. Jahn, T. R., O. S. Makin, …, L. C. Serpell. 2010. The common architecture of cross-β amyloid. *J. Mol. Biol.* 395:717–727.
19. Nelson, R., M. R. Sawaya, …, D. Eisenberg. 2005. Structure of the cross-β spine of amyloid-like fibrils. *Nature.* 435:773–778.
20. Petkova, A. T., Y. Ishii, …, R. Tycko. 2002. A structural model for Alzheimer's β-amyloid fibrils based on experimental constraints from solid state NMR. *Proc. Natl. Acad. Sci. USA.* 99:16742–16747.
21. Sekhar, A., and J. B. Udgaonkar. 2011. Fluoroalcohol-induced modulation of the pathway of amyloid protofibril formation by barstar. *Biochemistry.* 50:805–819.
22. Walsh, D. M., D. M. Hartley, …, D. B. Teplow. 1999. Amyloid β-protein fibrillogenesis. Structure and biological activity of protofibrillar intermediates. *J. Biol. Chem.* 274:25945–25952.
23. Walsh, D. M., A. Lomakin, …, D. B. Teplow. 1997. Amyloid β-protein fibrillogenesis. Detection of a protofibrillar intermediate. *J. Biol. Chem.* 272:22364–22372.
24. Jain, S., and J. B. Udgaonkar. 2010. Salt-induced modulation of the pathway of amyloid fibril formation by the mouse prion protein. *Biochemistry.* 49:7615–7624.
25. Kumar, S., and J. B. Udgaonkar. 2009. Structurally distinct amyloid protofibrils form on separate pathways of aggregation of a small protein. *Biochemistry.* 48:6441–6449.
26. Kumar, S., and J. B. Udgaonkar. 2009. Conformational conversion may precede or follow aggregate elongation on alternative pathways of amyloid protofibril formation. *J. Mol. Biol.* 385:1266–1276.
27. Campioni, S., B. Mannini, …, F. Chiti. 2010. A causative link between the structure of aberrant protein oligomers and their toxicity. *Nat. Chem. Biol.* 6:140–147.
28. Chimon, S., M. A. Shaibat, …, Y. Ishii. 2007. Evidence of fibril-like β-sheet structures in a neurotoxic amyloid intermediate of Alzheimer's β-amyloid. *Nat. Struct. Mol. Biol.* 14:1157–1164.
29. Haass, C., and H. Steiner. 2001. Protofibrils, the unifying toxic molecule of neurodegenerative disorders? *Nat. Neurosci.* 4:859–860.
30. Dobson, C. M. 2002. Getting out of shape. *Nature.* 418:729–730.
31. Uversky, V. N., and A. L. Fink. 2004. Conformational constraints for amyloid fibrillation: the importance of being unfolded. *Biochim. Biophys. Acta.* 1698:131–153.
32. Jha, A., J. B. Udgaonkar, and G. Krishnamoorthy. 2009. Characterization of the heterogeneity and specificity of interpolypeptide interactions in amyloid protofibrils by measurement of site-specific fluorescence anisotropy decay kinetics. *J. Mol. Biol.* 393:735–752.
33. Mukhopadhyay, S., P. K. Nayak, …, G. Krishnamoorthy. 2006. Characterization of the formation of amyloid protofibrils from barstar by mapping residue-specific fluorescence dynamics. *J. Mol. Biol.* 358:935–942.
34. Juneja, J., N. S. Bhavesh, …, R. V. Hosur. 2002. NMR identification and characterization of the flexible regions in the 160 kDa molten globule-like aggregate of barstar at low pH. *Biochemistry.* 41:9885–9899.
35. Gast, K., A. J. Modler, …, G. Damaschun. 2003. Effect of environmental conditions on aggregation and fibril formation of barstar. *Eur. Biophys. J.* 32:710–723.
36. Lomakin, A., D. B. Teplow, …, G. B. Benedek. 1997. Kinetic theory of fibrillogenesis of amyloid β-protein. *Proc. Natl. Acad. Sci. USA.* 94:7942–7947.
37. Kumar, S., S. K. Mohanty, and J. B. Udgaonkar. 2007. Mechanism of formation of amyloid protofibrils of barstar from soluble oligomers:

evidence for multiple steps and lateral association coupled to conformational conversion. *J. Mol. Biol.* 367:1186–1204.

38. Eftink, M. R. 1991. Topics in Fluorescence Spectroscopy. Plenum Press, New York.
39. Merkel, J. S., J. M. Sturtevant, and L. Regan. 1999. Sidechain interactions in parallel β sheets: the energetics of cross-strand pairings. *Structure.* 7:1333–1343.
40. Fooks, H. M., A. C. Martin, …, E. G. Hutchinson. 2006. Amino acid pairing preferences in parallel beta-sheets in proteins. *J. Mol. Biol.* 356:32–44.
41. Chan, J. C., N. A. Oyler, …, R. Tycko. 2005. Parallel β-sheets and polar zippers in amyloid fibrils formed by residues 10–39 of the yeast prion protein Ure2p. *Biochemistry.* 44:10669–10680.
42. Iwata, K., T. Fujiwara, …, Y. Goto. 2006. 3D structure of amyloid protofilaments of β2-microglobulin fragment probed by solid-state NMR. *Proc. Natl. Acad. Sci. USA.* 103:18119–18124.
43. Knowles, T. P., A. W. Fitzpatrick, …, M. E. Welland. 2007. Role of intermolecular forces in defining material properties of protein nanofibrils. *Science.* 318:1900–1903.
44. Perutz, M. F., T. Johnson, …, J. T. Finch. 1994. Glutamine repeats as polar zippers: their possible role in inherited neurodegenerative diseases. *Proc. Natl. Acad. Sci. USA.* 91:5355–5358.
45. Buck, M. 1998. Trifluoroethanol and colleagues: cosolvents come of age. Recent studies with peptides and proteins. *Q. Rev. Biophys.* 31:297–355.
46. Rajan, R., and P. Balaram. 1996. A model for the interaction of trifluoroethanol with peptides and proteins. *Int. J. Pept. Protein Res.* 48: 328–336.
47. Jasanoff, A., and A. R. Fersht. 1994. Quantitative determination of helical propensities from trifluoroethanol titration curves. *Biochemistry.* 33:2129–2135.
48. Blanco, F. J., M. A. Jiménez, …, J. L. Nieto. 1994. NMR solution structure of the isolated N-terminal fragment of protein-G B1 domain. Evidence of trifluoroethanol induced native-like β-hairpin formation. *Biochemistry.* 33:6004–6014.
49. Schönbrunner, N., J. Wey, …, T. Kiefhaber. 1996. Native-like β-structure in a trifluoroethanol-induced partially folded state of the all-β-sheet protein tendamistat. *J. Mol. Biol.* 260:432–445.
50. Yamaguchi, K., H. Naiki, and Y. Goto. 2006. Mechanism by which the amyloid-like fibrils of a β2-microglobulin fragment are induced by fluorine-substituted alcohols. *J. Mol. Biol.* 363:279–288.